The Astrophysical Journal, 985:194 (12pp), 2025 June 1 https://doi.org/10.3847/1538-4357/adc99e
© 2025. The Author(s). Published by the American Astronomical Society.
OPEN ACCESS

Traversing the Star-forming Main Sequence with Molecular Gas Stacks of $z \sim 1.6$ Cluster Galaxies

Alex Pigarelli[1,2,15], Allison Noble[1,2], Gregory Rudnick[3], William Cramer[1,4], Stacey Alberts[5], Yannick Bahe[6,7], Patrick S. Kamieneski[1], Sebastian Montaño[1], Adam Muzzin[8], Julie Nantais[9], Sarah Saavedra[1], Eelco van Kampen[10], Tracy Webb[11], Christina C. Williams[5,12], Gillian Wilson[13], and H. K. C. Yee[14]
[1] School of Earth & Space Exploration, Arizona State University, Tempe, AZ 85287, USA
[2] Beus Center for Cosmic Foundations, Arizona State University, Tempe, AZ 85287, USA
[3] The University of Kansas, Department of Physics and Astronomy, 1251 Wescoe Hall Drive, Lawrence, KS 66045, USA
[4] Department of Physics and Astronomy, Notre Dame University, South Bend, IN 46617, USA
[5] Steward Observatory, University of Arizona, 933 North Cherry Avenue, Tucson, AZ 85719, USA
[6] School of Physics and Astronomy, University of Nottingham, University Park, Nottingham NG7 2RD, UK
[7] Laboratory of Astrophysics, Ecole Polytechnique Fédérale de Lausanne (EPFL), Observatoire de Sauverny, 1290 Versoix, Switzerland
[8] Department of Physics and Astronomy, York University, 4700 Keele Street, Toronto, Ontario, ON MJ3 1P3, Canada
[9] Facultad de Ciencias Exactas, Departamento de Física y Astronomìa, Instituto de Astronomía, Fernández Concha 700, Edificio C-1, Piso 3, Las Condes, Santiago, Chile
[10] European Southern Observatory, Karl-Schwarzschild-Str. 2, 85748, Garching bei München, Germany
[11] Department of Physics, McGill Space Institute, McGill University, 3600 rue University, Montréal, Québec, H3A 2T8, Canada
[12] NSF National Optical-Infrared Astronomy Research Laboratory, 950 North Cherry Avenue, Tucson, AZ 85719, USA
[13] Department of Physics, University of California Merced, 5200 Lake Road, Merced, CA 95343, USA
[14] The David A. Dunlap Department of Astronomy and Astrophysics, University of Toronto, 50 St George Street, Toronto, ON M5S 3H4, Canada
Received 2024 December 17; revised 2025 March 24; accepted 2025 April 4; published 2025 May 23

Abstract

The cluster environment has been shown to affect the molecular gas content of cluster members, yet a complete understanding of this often subtle effect has been hindered due to a lack of detections over the full parameter space of galaxy star formation rates (SFRs) and stellar masses. Here, we stack CO(2–1) spectra of $z \sim 1.6$ cluster galaxies to explore the average molecular gas fractions of galaxies both at lower mass ($\log(M_*/M_\odot) \sim 9.6$) and further below the star-forming main sequence (SFMS; $\Delta\mathrm{MS} \sim -0.9$) than other literature studies; this translates to a 3σ gas mass limit of $\sim 7 \times 10^9\, M_\odot$ for stacked galaxies below the SFMS. We divide our sample of 54 $z \sim 1.6$ cluster galaxies, derived from the Spitzer Adaptation of the Red-Sequence Cluster Survey, into nine groupings, for which we recover detections in 8. The average gas content of the full cluster galaxy population is similar to coeval field galaxies matched in stellar mass and SFR. However, when further split by CO-undetected and CO-detected, we find that galaxies below the SFMS have statistically different gas fractions from the field scaling relations, spanning deficiencies to enhancements from 2σ below to 3σ above the expected field gas fractions, respectively. These differences between $z = 1.6$ cluster and field galaxies below the SFMS are likely due to environmental processes, though further investigation of spatially resolved properties and more robust field scaling relation calibration in this parameter space are required.

Unified Astronomy Thesaurus concepts: Galaxy clusters (584); High-redshift galaxy clusters (2007); Galactic and extragalactic astronomy (563); Radio astronomy (1338); Molecular gas (1073)

1. Introduction

It has been well established in the literature that a galaxy's environment has an impact on various galactic properties, including morphology (A. Dressler 1980; M. Postman & M. J. Geller 1984; A. Dressler et al. 1997) and star formation rate (SFR; A. Dressler 1984; I. Lewis et al. 2002; Y. J. Peng et al. 2010). In recent years, an abundance of molecular gas studies have also looked at the link between the environment and its impact on the gas properties of galaxies. Molecular gas, the raw fuel of star formation, provides a unique perspective on galaxy evolution as it probes future star formation in galaxies and it has been shown to be affected by cluster environments.

Historically, carbon monoxide (CO) has been used as a tracer of molecular gas in galaxies due to the difficulty of observing molecular hydrogen (P. M. Solomon & P. A. Vanden Bout 2005; C. L. Carilli & F. Walter 2013). In particular, several high-resolution studies at low redshift have investigated the molecular gas reservoirs in cluster galaxies: the Virgo Environment Traced in CO (T. Brown et al. 2021), the Atacama Large Millimeter/submillimeter Array (ALMA) Fornax Cluster Survey (N. Zabel et al. 2019), and the Gas Stripping Phenomena in galaxies survey (B. M. Poggianti et al. 2017). These surveys explored the environmental effects on cluster galaxies, with all finding evidence of a significant population of cluster galaxies with debris trails ("jellyfish galaxies"), and/or disturbed morphologies and kinematics, most likely as a result of ram pressure stripping (RPS; N. Zabel et al. 2019; A. Moretti et al. 2020a; N. Zabel et al. 2022).

Aside from morphological changes to the molecular gas in galaxies, environmental effects have also been observed to alter a galaxy's total gas content.[16] Some quenching mechanisms strictly remove gas from galaxies, but RPS has been observed to remove gas while also compressing gas on the leading edge

[15] Corresponding author.

Original content from this work may be used under the terms of the Creative Commons Attribution 4.0 licence. Any further distribution of this work must maintain attribution to the author(s) and the title of the work, journal citation and DOI.

[16] Details of environmental quenching mechanisms can be found in L. Cortese et al. (2021), A. Boselli et al. (2022), and S. Alberts & A. Noble (2022).

of the galaxy, which can create a favorable environment for molecular gas formation (B. Vollmer et al. 2012; P. Jáchym et al. 2017; W. J. Cramer et al. 2020, 2021; A. Moretti et al. 2020a; I. D. Roberts et al. 2022). RPS can therefore potentially increase the total molecular gas content of a galaxy so that it can be detected through either gas tails, as in jellyfish galaxies, or possibly through elevated gas content. One such example of RPS forming as well as removing molecular gas is the jellyfish JW100, where the total integrated molecular gas content of the galaxy and tail exceeds the molecular gas content of similar, undisturbed galaxies (A. Moretti et al. 2020a).

To detect deviations in integrated molecular gas content, one must compare observations of cluster galaxies to those of coeval field galaxies. Large samples of integrated CO in field galaxies across redshift are thus key to assessing the ubiquity of an environmental impact on molecular gas. Work by L. J. Tacconi et al. (2018, hereafter T18) found an empirically derived "field scaling relation" (see also R. Genzel et al. 2015) between a galaxy's redshift, stellar mass, SFR, and molecular gas mass among star-forming field galaxies. T18 used 1444 measurements of molecular gas at $0 < z < 4$ from many surveys and found that the relationship between the galaxy properties and molecular gas content had a fairly narrow scatter (0.2 dex for individual galaxies, 0.1 dex for averages of galaxies). Therefore, cluster galaxies can be classified as gas-deficient or gas-rich in relation to field galaxies of similar properties. However, the T18 relation was mainly created from galaxies with SFRs along and above the star-forming main sequence (SFMS). As such, the field scaling relation is not calibrated for galaxies below the SFMS and does not predict observed gas masses in quiescent galaxies (see C. C. Williams et al. 2021; K. E. Whitaker et al. 2021b).

For galaxies on and around the SFMS, the field scaling relation can be used to investigate trends of gas content in cluster galaxies over redshift. In S. Alberts & A. Noble (2022), this is depicted in their Figure 14 for CO measurements in cluster galaxies from $z \sim 0$ to 2. To summarize, in local clusters between $z = 0$ and 0.2, there is a wide range of gas content which spans ~2 dex below to ~0.5 dex above T18. At slightly higher redshift ($0.2 < z < 0.6$), integrated molecular gas measurements have similarly found cluster galaxies that are gas-deficient as well as galaxies that are gas-rich (J. E. Geach et al. 2009, 2011; R. Cybulski et al. 2016; G. Castignani et al. 2020; D. Spérone-Longin et al. 2021). At high redshift ($z > 1$), a majority of cluster galaxies are consistent with or gas-rich compared to the T18 field scaling relation, and unlike low redshift results, a population of significantly gas-deficient star-forming galaxies is notably absent (M. Aravena et al. 2012; J. Wagg et al. 2012; A. G. Noble et al. 2017, 2019; M. Hayashi et al. 2018; C. C. Williams et al. 2022; G. Rudnick et al. 2017). It is not known whether this result simply reflects limited CO sensitivity and Malmquist bias, or indicates a reversal of what has been observed in the local galaxy clusters.

In this paper, we address this problem by probing CO emission to fainter luminosities through stacking analyses with 54 galaxy cluster members in three $z \sim 1.6$ galaxy clusters from the Spitzer Adaptation of the Red-Sequence Cluster Survey (SpARCS; A. Muzzin et al. 2009; G. Wilson et al. 2009). These clusters are of particular interest as their members are known to have elevated gas fractions (A. G. Noble et al. 2019), high levels of kinematic asymmetries (W. J. Cramer et al. 2023), and a wide range of UV-optical color gradients (W. J. Cramer et al. 2024) compared to field galaxies. On the other hand, the cluster members have also been observed to have Hα emission similar to field galaxies (J. Nantais et al. 2020). We divide cluster members in different regions of the M_*–ΔMS (offset from SFMS) parameter space into groupings of all members, individually CO-detected members, and individually CO-undetected members to obtain the stacked spectra and average molecular gas masses of the galaxies in these bins. Comparing these gas masses to the T18 field scaling relation, we can assess whether the galaxies are, on average, influenced by environmental effects. The evidence of environmental effects could manifest through increased or decreased gas masses compared to coeval field galaxies.

We organize the paper as follows: Section 2 introduces the three $z \sim 1.6$ clusters and their observations, Section 3 presents the data preparation, Section 4 shows our analysis, Section 5 contains a discussion of our results, and Section 6 summarizes our conclusions. Throughout this paper, we adopt a Chabrier initial mass function and a ΛCDM cosmology with $H_0 = 70$ km s^{-1} Mpc^{-1}, $\Omega_M = 0.3$, and $\Omega_\Lambda = 0.7$.

2. Observations

2.1. SpARCS Clusters

In this paper, we explore the CO content of galaxies within three massive ($M_* \gtrsim 10^{14} M_\odot$) galaxy clusters at $z \sim 1.6$ (J. B. Nantais et al. 2016; A. G. Noble et al. 2017, 2019; W. J. Cramer et al. 2023): SpARCS J022416-032330 ("J0224"), SpARCS J022546-035517 ("J0225"), and SpARCS J033056-284300 ("J0330"). These clusters were identified with the Stellar Bump Sequence technique (A. Muzzin et al. 2013) and have been imaged in 18 photometric bands spanning UV/far-infrared (FIR). All clusters have ground-based ugrizYKs, 3.6/4.5/5.0/8.0/24.0 μm Spitzer imaging, and Hubble Space Telescope (HST) F160W. J0224 and J0330 also benefit from HST F105W and F140W imaging from the "See Change" program (B. Hayden et al. 2021). Optical and near-IR bands were point-spread function matched to the K_s-band images (J. B. Nantais et al. 2016). In addition, all clusters were a part of the XMM-LSS and CDFS fields imaged by the PACS and SPIRE instruments aboard Herschel, which have publicly available, deblended FIR catalogs (100/160/250/350/500 μm). These catalogs were deblended to match the resolution of the Spitzer MIPS 24 μm data (I. G. Roseboom et al. 2010; S. J. Oliver et al. 2012; A. J. Smith et al. 2012; L. Wang et al. 2014). A galaxy is considered a member of one of the clusters if it has a spectroscopic redshift that falls within $\Delta z_{\rm cluster} = \pm 0.015$ from the cluster redshift. Currently, 113 cluster members have been identified over all three clusters, primarily from their Hα emission (J. B. Nantais et al. 2016).

2.2. ALMA Observations

Each cluster was targeted with ALMA Band 3 to capture the CO(2–1) emission within ±3000 km s^{-1} of the clusters' systematic redshifts. For J0224 and J0330, we use single-epoch, spatially resolved measurement sets (project code: 2018.1.00974.S, PI: Noble) and for J0225, we combine two spatially resolved measurement sets (project codes: 2017.1.01228.S, 2021.1.01002.S, PI: Noble). The measurement sets have synthesized beams of approximately 0.″5 × 0.″4 (~4.2 × 3.4 kpc) and total integration times for the clusters are 2.91 and 3.33 hr for two separate pointings in J0224, 11.65 hr combined in a single pointing for J0225, and 3.94 hr in a single pointing for J0330. The imaging

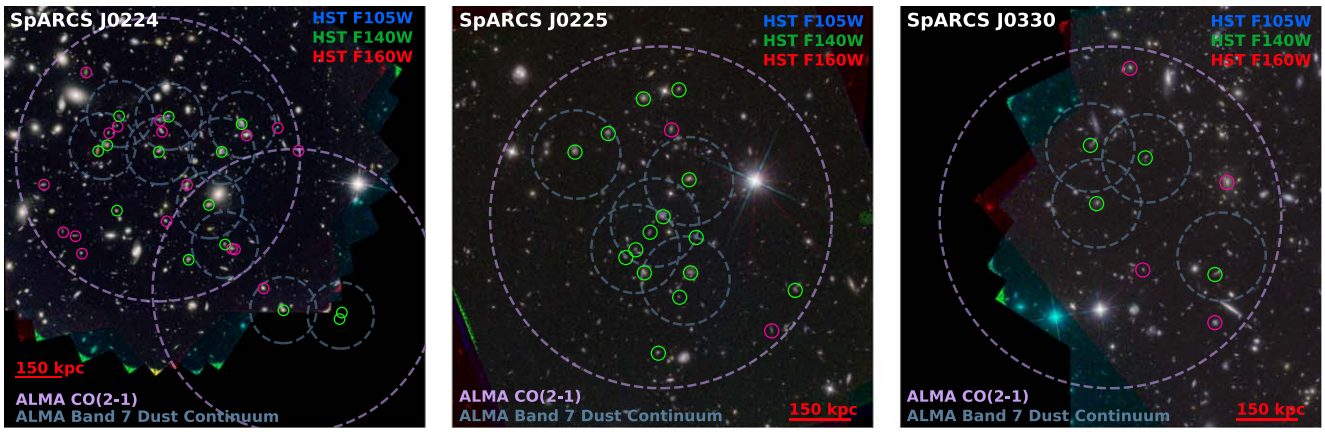

Figure 1. Shown above are the three SpARCS galaxy clusters used in this work. The background RGB images are created from HST F160W, F140W, and F105W imaging. The primary beams of the ALMA Band 3 CO(2–1) imaging and the ALMA Band 7 dust continuum imaging are shown by the purple and blue dashed circles, respectively. The green and pink circles denote the locations of the CO-detected and CO-undetected cluster members, respectively. See Section 3.1 for further details.

contains CO(2–1) detections of 32 cluster members, with an additional 22 spectroscopically confirmed cluster members not detected, but within the ∼95″ diameter primary beams. A cluster member was considered to be detected if it had a CO detection with a 3σ peak spanning more than two adjacent 50 km s^{-1} channels with a corresponding K_s-band counterpart.

We also use ALMA Band 7 dust continuum observations (project code: 2021.1.01257.S, PI: Noble), which cover 36 of the 54 cluster members present in the CO(2–1) imaging. Each of the 19 pointings spread across the three clusters was targeted at rest frame ∼330 μm and has ∼35–40 minutes of integration time with a central rms of 0.02 mJy beam^{-1}. The primary beam of these observations is ∼25″ and the median synthesized beam size is 0.″45 × 0.″37 (∼3.8 × 3.1 kpc).

Figure 1 shows HST imaging of each cluster used in this work, along with the primary beams of the ALMA Bands 3 and 7 observations with the CO detections and CO-non-detections notated.

3. Data

3.1. Band 3 CO(2–1) Reduction and Spectral Extraction

We reduce the ALMA measurement sets using the CASA ALMA Science Pipeline version 6.5.4.9 (J. P. McMullin et al. 2007). For the CO(2–1) observations, the two J0225 measurement sets are first concatenated and then the measurement sets of each cluster are uv-continuum subtracted and cleaned using `tclean` with natural weighting, a stopping threshold of 2.5σ, manual masking, primary beam response set to 20%, and primary beam correction enabled. The synthesized beams for the images are 0.″45 × 0.″35 for J0224, 0.″52 × 0.″41 for J0225, and 0.″48 × 0.″39 for J0330. Each image is created with a cell size chosen such that there are 8 pixels across the minor axis of each of the clean beams. The central rms in 50 km s^{-1} channels are 0.05 mJy beam^{-1}, 0.04 mJy beam^{-1}, and 0.07 mJy beam^{-1} for J0224, J0225, and J0330, respectively.

We measure the size of each CO-detected cluster member with the `imfit` task in `CASA`, which fits a 2D Gaussian profile, on velocity-integrated intensity maps (moment 0 maps) for each galaxy. These sizes and position angles are then used to create custom elliptical spectral extraction apertures for each galaxy at a radius of 4 * half width at half-maximum/2.355, enclosing the flux within 4σ. We additionally average the spectra of CO-undetected cluster members shifted to the rest frame to perform a curve of growth analysis and find the total flux from a Gaussian fit flattened beyond a circular aperture radius of 0.″8. We use this size aperture for spectral extraction of the CO-undetected galaxies.

3.2. Band 7 Dust Continuum Reduction and Flux Extraction

Each ALMA Band 7 pointing, centered at 345 GHz, was individually cleaned with `tclean` using a natural weighting, a stopping threshold of 2.5σ, manual masking, primary beam response set to 20%, and primary beam correction enabled. The minor axes of the clean beams are similar in size, which enables a uniform pixel size across the images of 0.″037, or ∼10 pixels across the minor axes. We use `imfit` at the locations of known cluster members to measure the integrated flux and require a signal-to-noise ratio (SNR) of greater than 3 to consider a cluster member detected. For undetected cluster members, we extract blank apertures at the same primary beam response as the cluster member to estimate the 3σ upper limit on the emission. While the Band 7 imaging has uniform depth in all pointings, the 3σ upper limits change per galaxy due to their location in the primary beams (e.g., sources closer to the edge have elevated 3σ limits as the primary beam correction increases the local pixel-to-pixel rms).

3.3. Stellar Masses and SFRs

We use the spectral energy distribution (SED) fitting code Code Investigating GALaxy Emission (`CIGALE`; M. Boquien et al. 2019) to estimate stellar masses and SFRs of the SpARCS cluster members with all available bands of photometry. We chose to use `CIGALE` for its optical-IR energy balance and ability to consider upper limits when sources were undetected in an imaging band. Due to the shallow HerMES imaging depth, when a source had no FIR emission in the catalog, an upper limit of the 3σ clipped rms noise was used for each band as described in I. G. Roseboom et al. (2010). For the population of SpARCS cluster members greater than 0.3 dex below the SFMS (three galaxies have $\log(M_*/M_\odot) <$ 10.0, 23 have $\log(M_*/M_\odot) >$ 10.0), the SFRs are constrained by having HerMES upper limits on their FIR emission. Of these galaxies, eight of 26 have ALMA Band 7 dust continuum detections with an average uncertainty on the measurements of 0.16 mJy and an average detection significance of 7.6σ. Seven of the 26 have ALMA Band 7 3σ upper limits with an average limit of 0.30 mJy. The remaining 11 galaxies were not contained in the

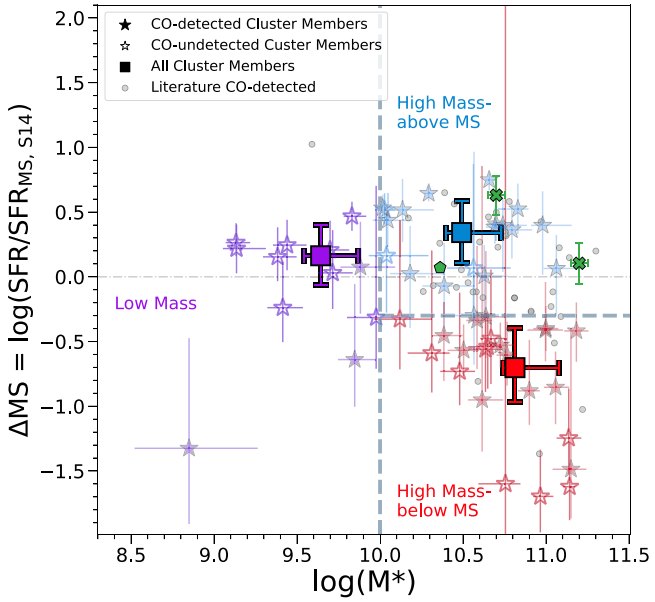

Figure 2. Our sample of cluster galaxies is shown with their stellar masses and offsets from the SFMS. CO-detected cluster members are shown with filled stars and CO-undetected cluster members with open stars. The averages of cluster members in the three groupings (LM, HM-aMS, and HM-bMS) are shown with the solid squares, with error bars representing the uncertainty on the mean. Comparison stacks of cluster members from M. Hayashi et al. 2018 (pentagon, $z = 1.46$) and S. Alberts et al. 2022 (crosses, $z \sim 1.4$) are shown by the dark green points. Gray circles indicate individual $z > 1$ literature cluster members (M. Aravena et al. 2012; G. Rudnick et al. 2017; R. T. Coogan et al. 2018; M. Hayashi et al. 2018; C. C. Williams et al. 2022).

ALMA Band 7 pointings and they only have their FIR emission constrained by the HerMES 3σ limits of 10.1 mJy, 10.8 mJy, and 14.5 mJy for the 250 μm, 350 μm, and 500 μm bands, respectively.

We assume an exponentially declining star formation history with BC03 simple stellar populations (G. Bruzual & S. Charlot 2003), a Chabrier initial mass function (G. Chabrier 2003), and Calzetti dust attenuation (D. Calzetti et al. 2000). The range of stellar masses from CIGALE spans $\log(M_*) = 8.8$–11.2 and SFRs span 0.1–$279 M_\odot$ yr^{-1} averaged over the last 100 Myr. In Figure 2, we show the distribution of stellar masses and offsets from the SFMS (J. S. Speagle et al. 2014, hereafter S14) of our galaxy sample as well as our grouping criteria of galaxy properties (presented in Section 4.1). In this parameter space, we also show $z > 1$ literature CO-detected galaxies and two other $z \sim 1.5$ literature stacking studies (M. Hayashi et al. 2018; S. Alberts et al. 2022) to illustrate that our work effectively probes new regions of M_*–ΔMS parameter space that other high-redshift cluster studies have not. We note that a vast majority of literature CO-detected galaxies at $z > 1$ (28 of 35) fall into the upper right portion of this parameter space (see Figure 2), which includes high-mass star-forming galaxies. Meanwhile, 35 of our 54 SpARCS cluster members (~65%) are outside of this high-mass star-forming classification.

4. Analysis

4.1. Spectral Stacking

With the extracted spectra from the CO(2–1) image cubes as described in Section 3.1, we shift the spectra to the rest frame based on their CO redshift, when available, or Hα spectroscopic redshift (J. B. Nantais et al. 2016). We then interpolate the spectra to common 50 km s^{-1} velocity bins, average the interpolated spectra, and perform an initial χ^2 Gaussian fit to generate a $\pm 5\sigma$ bound on the emission line velocity center. A line-free channel-to-channel rms value is calculated for each spectrum outside of the $\pm 5\sigma$ bounds, which provides the weightings for each spectrum when they are stacked with inverse-variance weighting. We apply these same weightings when calculating the weighted average stellar masses and weighted average SFRs.

We then separate the spectra into three groupings based on stellar mass and offset from the SFMS and stack the spectra in each grouping with inverse-variance weighting according to their line-free channel-to-channel rms. S14 reports the scatter on a majority of literature SFMS fits to be between 0.2 and 0.3 dex (T18 reports this conservatively as 0.3 dex). To preserve a pristine sample of galaxies below the SFMS, we adopt a scatter of 0.3 dex on the SFMS and classify cluster members greater than 0.3 dex below the Main Sequence to be "below Main Sequence" (bMS) galaxies. For our first classification, all galaxies with a stellar mass of $\log(M_*/M_\odot) < 10.0$ are assigned to the Low Mass group (LM grouping). Galaxies with stellar masses of $\log(M_*/M_\odot) > 10.0$ that are above or consistent with the SFMS ($\Delta\text{MS} > -0.3$) are considered High Mass above-SFMS galaxies (HM-aMS grouping). While not all galaxies in this grouping are actually above the SFMS, only three are below, and 13 of 19 galaxies have offsets greater than +0.3 dex (see Figure 2). The remaining galaxies that are above $\log(M_*/M_\odot) > 10.0$ and more than 0.3 dex below the SFMS are considered part of the High Mass-below-SFMS grouping (or HM-bMS). We note that our results are insensitive to adjusting the below Main Sequence classification to any measurement below the Main Sequence (<0 dex offset) and choose to keep our classification limit at <-0.3 dex offset for a more pristine sample of bMS galaxies. Both the LM and HM-bMS classifications described here represent relatively unstudied high-redshift cluster populations (see Figure 2 with one literature cluster member in the LM grouping and six in the HM-bMS grouping) and therefore provide new insight into the molecular gas masses of cluster members.

The above classifications assign three CO-detected and nine CO-undetected galaxies to the LM grouping, 16 CO-detected and three CO-undetected galaxies to the HM-aMS grouping, and, remarkably, 13 CO-detected and 10 CO-undetected galaxies to the HM-bMS grouping. We create inverse-variance weighted stacked spectra for each of the three classifications of galaxies, as well as inverse-variance weighted stacks of spectra for the CO-detected and CO-undetected galaxies within each of the groupings for comparison.

4.2. Spectral Bootstrapping

We account for the variance of our sample of cluster galaxies and photometric uncertainty by bootstrapping our inverse-variance weighted stacked spectra. In our bootstrapping, we first randomly select the same number of spectra as there are in each grouping, allowing for repetition, and apply inverse-variance weighting to the constituent spectra to create a new "bootstrapped" spectrum. This creates a single new realization of our data. We do not allow for re-mixing of the spectra, such that spectra from the LM grouping are not selected in any of the other groupings and vice versa. This bootstrapping is performed with 1000 realizations per grouping and the standard

deviation in each channel across all realizations gives the uncertainty of the flux for each channel (e.g., the standard deviation of the 1000 realizations in the -100 km s^{-1} channel gives the 1σ uncertainty on the -100 km s^{-1} channel). We use these uncertainties with the non-bootstrapped stacked spectra and each bootstrapped realization for integrated flux measurements with a Bayesian fitter (see Section 4.3).

We note that the uncertainty from the bootstrapping does not yield the final uncertainty on our measured gas masses but constitutes the spectral uncertainty for Bayesian fitting as described in Sections 4.3 and 4.4. Additionally, the number of bootstraps performed does not affect the significance of our final detections as long as there is sufficient sampling of the constituent spectra in each grouping. In line-free channels, the uncertainty on the flux measurements from this methodology accounts for the photometric uncertainty, essentially the equivalent of stacking blank apertures. In channels where there is emission, the bootstrapping simultaneously accounts for both photometric uncertainty and variance of CO flux from the galaxies.

We assume that any channel-to-channel correlated noise is minimal and does not impact the spectra. The native velocity resolutions of the ALMA observations are $\sim$13 km s^{-1}, which gives approximately four native channels mapped to each 50 km s^{-1} final channel. We bin our final images at 50 km s^{-1} to increase the SNR in each channel while still having a sufficient number of velocity channels for adequate Gaussian emission line fitting and to be consistent with previously published work on these measurement sets (see A. G. Noble et al. 2019; W. J. Cramer et al. 2023). While the native velocity resolutions are not perfect integer multiples of the final velocity resolution, we assume that the large number of native channels mapped to final channels is sufficient to not need to consider channel-to-channel correlated noise (see further discussion of spectral regridding and rebinning in A. K. Leroy et al. 2021).

4.3. Bayesian Fitting of Stacked Spectra

We model a Gaussian emission line using the `dynesty` package (J. S. Speagle 2020) to perform nested sampling fits to the observed stacked spectra (described in Section 4.2) shown in Figure 3. The prior bounds on our Gaussian emission line fit are velocity centroid $\in$ ($-$300,300) km s^{-1}; centroid amplitude $\in$ (0.00, 1.50) mJy; and FWHM $\in$ (0.01,500) km s^{-1}. We assign a uniform prior to the amplitude parameter, and Gaussian priors to the centroid and FWHM parameters. For the centroid prior, we set $\sigma = 63.7$ km s^{-1} centered at 0 km s^{-1}. We perform initial χ^2 fits to the three "all" groupings to inform the FWHM priors. For the LM grouping, we set the Gaussian prior on the FWHM to be centered on 300 km s^{-1} with $\sigma = 31$ km s^{-1}. We give the HM-aMS grouping a Gaussian FWHM prior centered on 365 km s^{-1} with a width of 21 km s^{-1}, and the HM-bMS a Gaussian FWHM prior centered on 407 km s^{-1} with a width of 61 km s^{-1}.

We use this Bayesian fitter to also measure the uncertainty on the flux due to population variance. To do this, we fit the 1000 bootstrap realizations in each grouping along with the bootstrapped channel-to-channel 1σ uncertainties (see Section 4.2) with the Bayesian nested sampler to obtain the posterior distribution of areas under the Gaussian curves. This quantifies the range of possible fluxes present in each grouping. Second, we use the observed (non-bootstrapped) weighted spectra, with the same channel-to-channel 1σ bootstrapping uncertainties, with the Bayesian fitter to measure the average flux of the galaxies in each grouping. In this way, we report a flux measured from the observed stacked spectrum in each grouping, as well as the 1σ range of bootstrapped fluxes, each measured independently with a Gaussian. This range of bootstrapped fluxes is not equivalent to a detection significance, but flux uncertainty due to population variance. As such, we also report a nonparametric emission significance for each observed stacked spectrum, which uses the number of emission channels and the rms in line-free channels to assess the significance of emission as shown below (F. Sinigaglia et al. 2022):

$$\mathrm{SNR} = \frac{\sum_i^{N_{\mathrm{ch}}} S_i \Delta v}{\sigma_{\mathrm{rms}} \Delta v \sqrt{N_{\mathrm{ch}}}} \quad (1)$$

where N_{ch} is the number of channels with emission, S_i is the flux in each channel, Δv is the velocity width of each channel, and σ_{rms} is the line-free channel-to-channel rms. We show the nonparametric emission significance for each grouping in Figure 3.

4.4. Gas Masses

We follow the P. M. Solomon & P. A. Vanden Bout (2005) method of calculating the CO line luminosity:

$$L'_{\mathrm{CO}} = 3.25 \times 10^7 * S_{\mathrm{CO}} \Delta_\nu * \frac{D_L^2}{\nu_{\mathrm{rest}}^2 (1+z)} [\mathrm{K\ km\ s^{-1}\ pc^2}] \quad (2)$$

where $S_{\mathrm{CO}}\Delta_\nu$ is the velocity-integrated flux in Jy km s^{-1}, D_L is the luminosity distance in Mpc, and ν_{rest} is the rest frequency of 230.54 GHz. The line luminosity can be converted into a gas mass through

$$\frac{M_{\mathrm{gas}}}{M_\odot} = \alpha_{\mathrm{CO}} \frac{L'_{\mathrm{CO}}}{r_{21}}. \quad (3)$$

Here, we adopt an excitation factor correction, r_{21}, of 0.77 (E. Daddi et al. 2015; R. Genzel et al. 2015). The value of the CO-to-H_2 conversion factor, α_{CO}, is difficult to measure outside the Milky Way, and some studies have found it to be metallicity dependent (D. Cormier et al. 2014). T18 uses a metallicity correction for α_{CO} based on either the observed 12 +log(O/H) or a prescription to obtain metallicity from stellar mass and redshift. We do not have metallicity estimates for all CO-detected galaxies in our clusters, but those with measured metallicities fall roughly in the range of 12+log(O/H) between $\sim$8.4 and 8.7 as estimated from [N II]/Hα ratios (J. Nantais et al. 2025, in preparation). Therefore, we rely on a stellar mass–metallicity correction to α_{CO} for all of our cluster members. We find the weighted average α_{CO} for our stacks of spectra to be between 4.4 and 6.9 [$(M_\odot$ km s^{-1} pc$^{-2})^{-1}$] (see Figure 3).

With the output from the Bayesian parameter fitting and the assumptions listed above, we detect average gas masses of 1.2 +0.9/-0.6 $\times 10^{10}\ M_\odot$, 6.3+1.3/-1.1 $\times 10^{10}\ M_\odot$, and 3.3 +1.2/-0.8 $\times 10^{10}\ M_\odot$ for the LM, HM-aMS, and HM-bMS groupings. These gas masses correspond to gas fractions ($f_{\mathrm{gas}} = M_{\mathrm{gas}}/(M_{\mathrm{gas}} + M_*)$) of 75%+15/-13%, 67% +6/-8%, and 34% +9/-7%, respectively. Average properties and gas properties of all groupings of galaxies are presented in Table 1. We compute the offset from the T18 field scaling relation (ΔT18)

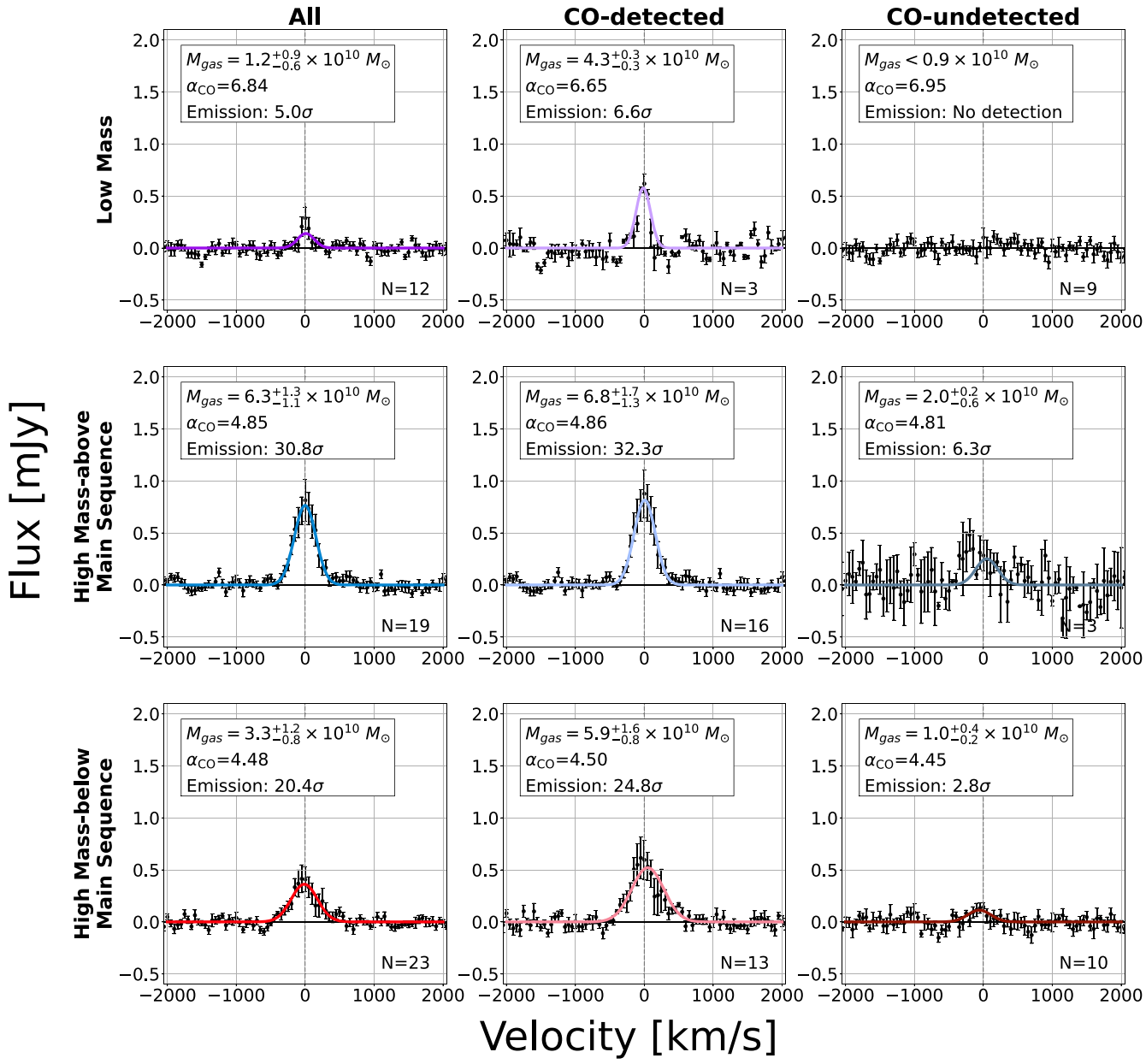

Figure 3. The inverse-variance weighted stacked spectra of LM (top row), HM-aMS (middle row), and HM-bMS (bottom row) groupings. In each case, the left-hand panel shows the full stack, while the middle and right-hand panels only include CO-detected and CO-undetected galaxies, respectively. In each panel (except the LM CO-undetected grouping in the top-right corner), the best-fit Gaussian is shown by the solid curve. Stellar masses, SFRs, integrated fluxes, and gas fractions of each grouping are shown in Table 1. We report the nonparametric significance of emission in each spectrum as well as the measured gas mass and variance from bootstrapped realizations in each grouping; see Section 4.3 for details.

as the log gas-to-stellar ratio offset ($\mu = M_{\rm gas}/M_*$; ΔT18 = $\log(\mu_{\rm measured})$–$\log(\mu_{\rm T18})$) for each grouping of galaxies given their redshift, stellar mass, and SFRs and also present them in Table 1.

4.5. Gas Detection Limits

We investigate the upper limit of gas content that we are able to detect by simulating a flat spectrum, adding a known amount of flux to the spectrum in the form of a Gaussian emission line, adding noise to the data, adding error bars to each channel, and finally attempting to recover the injected flux through the same Bayesian parameter estimation as Section 4.3. We run a full grid of parameters where we vary the channel-to-channel noise of the spectrum, the magnitude of the error bars, and the known amplitude and FWHM of the simulated emission line.

To measure the smallest integrated flux we are sensitive to, given the noise properties of our spectra, we first filter the grid of parameters to match the properties of our stacked spectra. For each grouping, we select a subset of all the simulated spectra with channel-to-channel noise and error bar magnitude input grid points similar to those of the measured quantities of the weighted spectra. We then compare the signal-to-noise of the Bayesian recovered flux to the injected flux and find the lower limit on the injected flux where 90% of the stacked spectra have a 3σ detection. We consider this flux to be our 3σ completeness limit. Figure 4 shows the SNR of the recovered flux as a function of the injected flux from the subset of simulated spectra with noise properties similar to the HM-aMS CO-undetected grouping. Starting on the right side of the plot,

Table 1
A Summary of the Weighted Average Properties from CIGALE SED Fitting and Spectral Measurements

Stack	N_{gal}	Stellar Mass ($\times 10^{10}$ $M_\odot$)	SFR ($M_\odot$ yr $^{-1}$)	Integrated Flux[a] (Jy km s^{-1})	Gas Mass ($\times 10^{10}$ $M_\odot$)	f_{gas}[b]	ΔT18[c]
LM-all	12	$0.4^{+0.1}_{-0.1}$	13^{+4}_{-3}	$0.04^{+0.03}_{-0.02}$	$1.2^{+0.9}_{-0.6}$	73^{+15}_{-13}%	0.09
LM-CO	3	$0.5^{+0.2}_{-0.1}$	7^{+4}_{-4}	$0.15^{+0.01}_{-0.01}$	$4.3^{+0.3}_{-0.3}$	90^{+3}_{-4}%	0.82
LM-no CO	9	$0.4^{+0.1}_{-0.1}$	16^{+4}_{-3}	<0.03	<0.9	<67%	−0.24
HM-aMS-all	19	$3.1^{+0.9}_{-0.7}$	78^{+17}_{-16}	$0.30^{+0.06}_{-0.06}$	$6.3^{+1.3}_{-1.1}$	67^{+6}_{-8}%	0.13
HM-aMS-CO	16	$3.1^{+0.8}_{-0.6}$	82^{+11}_{-16}	$0.31^{+0.08}_{-0.06}$	$6.8^{+1.7}_{-1.3}$	69^{+7}_{-7}%	0.14
HM-aMS-no CO	3	$3.3^{+1.6}_{-1.2}$	47^{+67}_{-19}	$0.10^{+0.01}_{-0.03}$	$2.0^{+0.2}_{-0.6}$	39^{+9}_{-14}%	−0.24
HM-bMS-all	23	$6.5^{+1.2}_{-1.0}$	15^{+8}_{-6}	$0.17^{+0.06}_{-0.04}$	$3.3^{+1.2}_{-0.8}$	34^{+9}_{-7}%	0.17
HM-bMS-CO	13	$6.2^{+1.2}_{-1.1}$	15^{+7}_{-6}	$0.30^{+0.08}_{-0.04}$	$5.9^{+1.9}_{-0.8}$	49^{+8}_{-6}%	0.40
HM-bMS-no CO	10	$7.0^{+1.2}_{-1.0}$	12^{+8}_{-6}	$0.05^{+0.02}_{-0.01}$	$1.0^{+0.4}_{-0.2}$	12^{+5}_{-3}%	−0.32

Notes.
[a] The integrated flux under a Gaussian fit to the stacked spectrum of galaxies. The uncertainties reported correspond to the 1σ bootstrapped variance of realizations of the grouping; see Section 4.2.
[b] $f_{gas} = M_{gas}/(M_{gas} + M_*)$.
[c] ΔT18 = log($\mu_{measured}$)–log(μ_{T18}); $\mu = M_{gas}/M_*$.

we take a vertical slice with a width of 2 mJy km s^{-1} and check the percentage of simulated spectra in that slice with an SNR greater than 3. If more than 90% of the simulated spectra in the slice have an SNR on the flux measurement greater than 3, we move one slice to the left and repeat until a slice no longer has 90% of the simulated spectra above an SNR of 3. For the HM-aMS CO-undetected grouping, this completeness limit occurs at 36 mJy km s^{-1}.

For our "all" groupings of galaxies, we measure sensitivity limits of +0.04, −0.76, and −0.46 dex relative to the T18 relation for the LM, HM-aMS, and HM-bMS groupings of galaxies at their weighted average stellar masses and ΔMS. Similarly, the CO-detected groupings of galaxies have ΔT18 limits of +0.05, −0.77, and −0.49 dex. And finally, the CO-undetected groupings have limits of −0.04, −0.70, and −0.41 dex. These detection limits, when using the assumptions in Section 4.4, correspond to $\sim$0.9–1 $\times$ 10^{10} $M_\odot$ for the LM groupings, $\sim$0.7–0.8 $\times$ 10^{10} $M_\odot$ for the HM-aMS groupings, and $\sim$0.7 $\times$ 10^{10} $M_\odot$ for the HM-bMS groupings.

4.6. Forward Modeling

To determine whether our measured gas fractions are consistent with coeval field galaxies, we employ a forward modeling technique to account for the distribution of galaxy properties within each grouping. We accomplish this by modeling the stellar masses and SFMS offsets of our cluster galaxies, drawing new realizations of the galaxy properties, and inputting them into the T18 field scaling relation to mimic field-like gas fractions. For each grouping, we take the measured stellar masses and SFMS offsets (ΔMS) of each individual galaxy in the grouping and draw a new value within the asymmetric errors 10,000 times. Just as we do with the spectral bootstrapping, we then select the same number of new mock stellar masses and mock ΔMSs from the sets of drawn values as are in the original grouping, allowing for repetition. We average these selected values to create a new realization of the measured quantities of our data. We repeat this 10,000 times for each grouping, such that we have a large number of realizations of our data. Using the average redshift of the groupings ($z = 1.6$), the newly sampled stellar masses, and newly sampled ΔMS, we are able to calculate a field-like gas fraction for each new grouping of coeval field galaxies In this way, we create a sample of galaxy properties similar to our cluster galaxies and obtain mock field-like gas fractions from the T18 relation. We Gaussian scatter the quantity log(μ) for each realization of "field galaxy groupings," assuming the inherent 0.1 dex scatter on the T18 relation.[17] If the measured gas fractions and uncertainties of our groupings are consistent with the mock "field galaxy distributions," we conclude that the stack is similar to field galaxies; otherwise, we conclude that

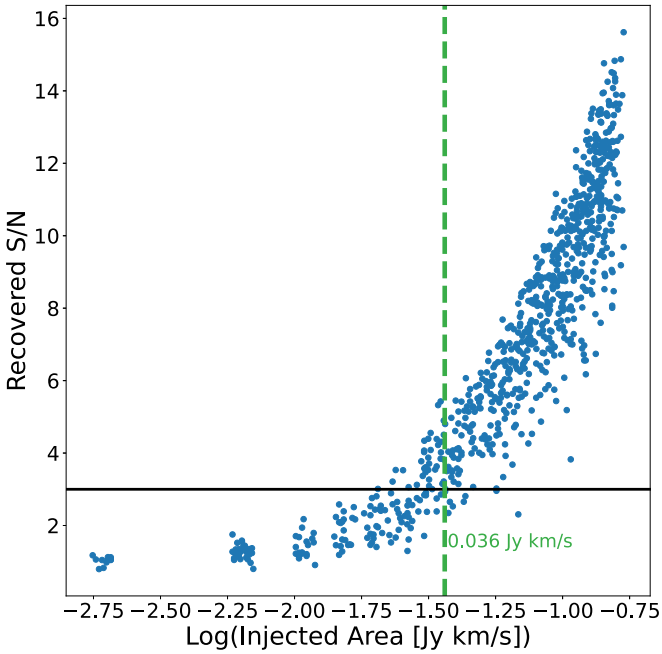

Figure 4. The scatter of recovered SNR as a function of flux injected into a flat spectrum with spectral noise properties similar to our CO-undetected HM-aMS grouping. We find our 3σ completeness limit to be 0.036 Jy km s^{-1} for this grouping using the procedure described in Section 4.5.

[17] 0.1 dex scatter on the T18 relation for averages of multiple galaxies, 0.2 dex scatter on the relation for individual galaxies.

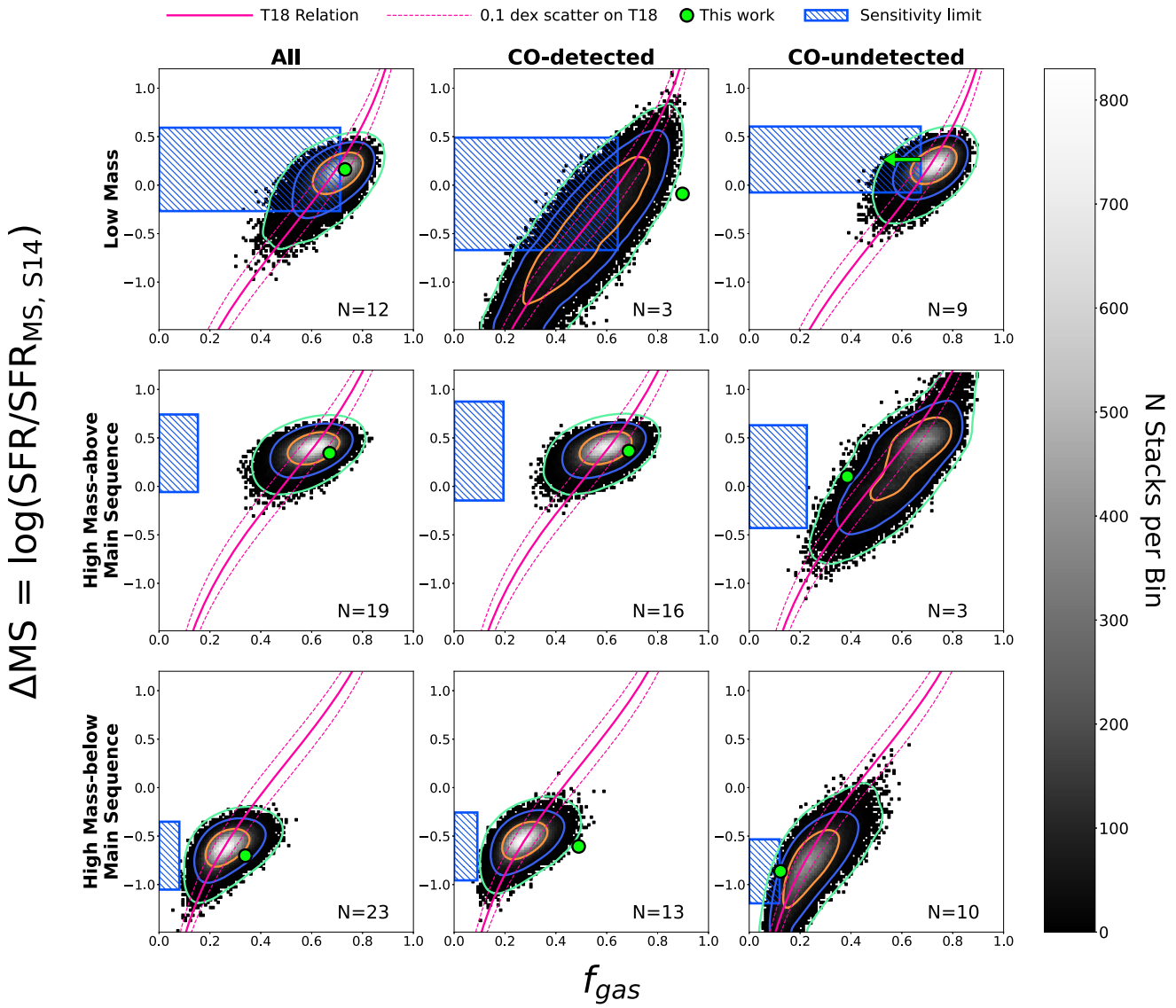

Figure 5. A comparison of our gas fraction measurements to forward-modeled stacks of coeval field galaxies. The 2D histograms in the background of the above plots show the distribution of gas fractions of forward-modeled "field galaxy" groupings as described in Section 4.6. The variance among constituent group members and each stellar mass and/or ΔMS measurements dictates the spread of these histograms in both the x and y-directions. The green point in each plot shows the measured SFMS offset (ΔMS) and gas fraction of each of our groupings, and the solid pink curve shows the mean field scaling relation for each of our groupings (for the average mass and SFR). The dashed pink lines represent the inherent 0.1 dex scatter on $\log(M_{gas}/M_*)$ of the field scaling relations. We show the contours that encompass 68% (1σ, orange), 95% (2σ, purple), and 99% (3σ, green) of groupings of field galaxies. The blue hatched region in each plot shows our sensitivity limit in f_{gas} and the vertical extent depicts the error on the mean ΔMS for each grouping.

the groupings of cluster members are either gas-rich or gas-deficient. We show the forward-modeled field galaxy distributions and our measured quantities in Figure 5.

5. Discussion

5.1. Comparison to Field and Literature

Looking at the groupings as a whole in Figure 5, we see that different populations of galaxies in the clusters exhibit both rich and deficient gas fractions. In this section, we examine our groupings column by column in Figure 5, compare the CO-detected stacks to the CO-undetected stacks, discuss the implications of scatter on values of α_{CO}, and finally compare the results of our stacking technique to the results of other intermediate-redshift and high-redshift CO and dust continuum stacking papers.

5.1.1. "All" Groupings

Generally, we see that the "all" groupings (left column), which include both CO-detected and spec-z confirmed CO-undetected cluster members, are contained within the 1σ contour of forward-modeled field-like galaxies. Despite having slight offsets from the field scaling relation (pink curves) for their weighted average stellar masses and ΔMS, this indicates that, on average, cluster members do not systematically show signs of being gas-deficient or gas-rich compared to equivalent field galaxies, regardless of stellar mass or ΔMS. This result is notable given that the T18 field scaling relation was primarily calibrated with galaxies similar in properties to our HM-aMS grouping, and that averages of all cluster galaxies, regardless of stellar mass and ΔMS, do not deviate from the relation. This

indicates that on average they are consistent as a population with field galaxies.

5.1.2. CO-detected Groupings

Among the individually CO-detected cluster members (center column), only the HM-aMS grouping contains galaxies that are solidly consistent with field-like gas fractions. This is not wholly unexpected given the similarity in stellar masses and ΔMS of our cluster members in this grouping to the field galaxies used in the calibration in T18. The LM and HM-bMS groupings, however, have gas fractions $>3\sigma$ above field predictions from T18. These findings are consistent with those of A. G. Noble et al. (2017, 2019), who focused only on the individually CO-detected cluster members. While it is impossible to narrow down the environmental effects on these groupings from their integrated gas mass measurements alone, these results could be indicative of enhanced molecular gas formation as a result of RPS (A. Moretti et al. 2020a, 2020b), inefficient star formation, or gas compression (see L. Cortese et al. 2021 for further discussion).

5.1.3. CO-undetected Groupings

Given the field-like and gas-rich detections within the CO-detected groupings, it is unsurprising that the CO-undetected galaxies (right column) generally show gas deficiencies. The LM CO-undetected grouping (top-right panel) presents an upper limit, but the limit includes a portion of field galaxy stacks at the 1σ level. We are unable to speculate what this upper limit could mean, as it only rules out the cluster members being gas-rich or consistent to within 1σ of the field scaling relation. The two remaining HM groupings have below field-like gas fractions at the $\sim 2\sigma$ level. These represent the first stacked gas mass detections for CO-undetected, high-redshift, cluster galaxies in this region of M_*–ΔMS parameter space (see Figure 2) and yet fail to find a significantly gas-deficient (more than 0.5 dex below the field scaling relation) population (-0.22 and -0.30 dex below T18, respectively). This result is significant because clusters at lower redshifts ($z < 1$) have an established population of significantly gas-deficient members over the same range of ΔMS that is probed at high redshift. However, six of the 10 galaxies in the CO-undetected HM-bMS grouping have the FIR portion of their SED constrained only by HerMES 250/350/500 μm upper limits (galaxies outside of our ALMA dust continuum imaging). These galaxies may have SFRs that are higher than currently estimated, which may place them in the HM-aMS grouping. Moving those galaxies out of the HM-bMS grouping could decrease the stacked CO emission, resulting in a more gas-deficient population of galaxies.

5.1.4. Comparison of CO-detected to CO-undetected in the bMS Bins

One of the most striking results in these stacks is the dichotomy between the deficiency and enhancement of gas fractions in the HM-bMS CO-undetected and CO-detected groupings from forward-modeled field galaxies (-2σ and $+3\sigma$). Again, we note that the T18 field scaling relation is primarily calibrated for galaxies on or above the SFMS at this redshift. This signifies a need for gas mass measurements of field galaxies below the SFMS, especially at $z > 1$. This makes interpretation challenging, but we add that most galaxies in the HM-bMS grouping have Main Sequence offsets within 1 dex of that in T18, such that we are not comparing quiescent galaxies, for which the field scaling relation does not hold, to field galaxies.

The stark difference between the CO-detected and CO-undetected stacks has been seen before in massive quiescent galaxies (J. Spilker et al. 2018; C. C. Williams et al. 2021; K. E. Whitaker et al. 2021b). While we do not definitively classify our galaxies as passive/quiescent due to their observed Hα emission and position in the UVJ diagram, our HM-bMS CO-detected and CO-undetected galaxies have very similar stacked Main Sequence offsets (ΔMS $= -0.60$ and -0.86, respectively) to the CO-detected and CO-undetected massive quiescent galaxies from J. Spilker et al. 2018 ($z \sim 0.7$, ΔMS ~ -0.7, and ~ -0.9, respectively). In contrast to the gas enhancement of our HM-bMS CO-detected grouping, the CO-detected massive quiescent galaxies are consistent with those in T18. However, both our HM-bMS CO-undetected grouping and the CO-undetected massive quiescent galaxies are below T18 and preserve the same ΔT18 ~ 0.7 dex separation from their CO-detected counterparts. As J. Spilker et al. (2018) suggest, this potentially suggests a break in the scaling relations for galaxies significantly below the SFMS, or alternatively, differing environmental effects between the two populations.

For example, in the HM-bMS CO-undetected grouping, the deficient molecular gas fractions could indicate gas-removal mechanisms such as strangulation or RPS in a purely gas-removal mode. The lack of gas in these galaxies could also be explained through the same gas consumption mechanisms that occur in quiescent or post-starburst field galaxies. In field studies of post-starburst galaxies, the molecular gas content of galaxies is thought to be tied to age; galaxies with ages less than 150 Myr can still have appreciable amounts of CO, but galaxies with ages greater than 150 Myr are remarkably devoid of CO (R. Bezanson et al. 2022; C. Woodrum et al. 2022). We are unable to reliably measure the ages of our cluster members without spectra of the D_n4000 break.

Contrary to the CO-undetected grouping, the CO-detected stack is gas enhanced, which could stem from inefficient star formation (T18 is sensitive to offset from the SFMS) or efficient molecular gas formation due to gas compression or perturbed gas from RPS (e.g., A. Moretti et al. 2020b). While literature studies have suggested that massive galaxies are more resistant to hydrodynamical environmental processes (J. E. Gunn & G. J. Richard 1972; L. L. Cowie & A. Songaila 1977; P. E. J. Nulsen 1982), massive galaxies in the local universe have exhibited gas enhancement in RPS stripped tails (jellyfish galaxies, e.g., A. Moretti et al. 2020a). Varying stages of RPS also show connections with the SFR of the disk or tails of the galaxies (I. D. Roberts & L. C. Parker 2020), and specifically, a connection has been observed between enhanced molecular gas in a galaxy's disk and star formation occurring in the RPS tail (A. Moretti et al. 2023). Future work will focus on spatially resolved studies of the molecular gas in our cluster galaxies to look for asymmetries associated with RPS.

5.1.5. Variance of α_{CO}

Another pertinent consideration in these interpretations is the impact of the variance of α_{CO} within galaxies and among galaxy populations. Historically, α_{CO} has been calibrated in the Milky Way as 4.36 $[(M_\odot \text{ km s}^{-1} \text{ pc}^{-2})^{-1}]$, but has also been shown to have dependence on galaxy metallicity and stellar mass surface densities (A. D. Bolatto et al. 2013). For all

groupings in this work, we need to increase the value of α_{CO} from the Milky Way 4.36 as a result of our stellar mass–metallicity correction (see Figure 3). Generally, the α_{CO} correction does not change the significance of the offset from the field scaling relations and increases the ΔT18 value for each grouping by 0.1 dex or less.

Nevertheless, we consider what values of α_{CO} would be required for our measured CO luminosities to be in line with the T18 field scaling relation. Most significantly, the HM-bMS CO-detected grouping would require an α_{CO} value of 1.74, and the HM-bMS CO-undetected grouping would need an α_{CO} value of 8.81 to be consistent with coeval field galaxies. Broadly, low values of α_{CO} are associated with starburst-type galaxies, which are not representative of the bMS galaxies, and high values of α_{CO} are associated with low-mass/low-metallicity galaxies (A. D. Bolatto et al. 2013). An α_{CO} value of 8.81 for our CO-undetected HM-bMS grouping would require a 12+log(O/H) metallicity of ∼8.34, which is unlikely for galaxies with $\log(M_*/M_\odot) = 10.84$. The disjointed characteristics of high and low values of α_{CO} and the high stellar mass with ΔMS below the SFMS indicate that environmental effects are altering the gas content in these galaxies. However, without metallicity information for all cluster members or CO spectral line energy distributions, we cannot unravel the full picture of molecular gas in these cluster galaxies.

5.2. Stacking Analyses Comparison

Similar to this work, M. Hayashi et al. (2018) performed a stacking analysis on 12 $z = 1.46$ star-forming cluster galaxies with spectroscopic redshifts, but without CO detections. The constituent galaxies in this stack are distributed in a similar region on the UVJ diagram as the low mass galaxies in this work (see Figure 6, dark green points outside the quiescent wedge). The average stellar mass of their star forming without CO group is similar to our LM groupings ($0.6 \times 10^{10} M_\odot$ and $0.4–0.5 \times 10^{10} M_\odot$ for our LM groupings). No detection is found for their stacked spectrum, whereas we find detections for two of our three LM groupings. The difference in the non-detection from M. Hayashi et al. (2018) is not unexpected, as the depth of the SpARCS CO(2–1) images is ∼10× deeper (∼0.01 mJy beam^{-1} versus 0.12 mJy beam^{-1} in 400 km s^{-1} channels). M. Hayashi et al. (2018) place a 5σ gas mass detection limit on their stacked spectrum of star forming without CO detections at $1.05 \times 10^{10} M_\odot$ ($f_{gas} < 62\%$), whereas we find detections on the LM "all" and CO-detected groupings of 1.3 and 4.3 $\times 10^{10} M_\odot$ ($f_{gas} = 75\%$ and 90%, respectively). The 3σ detection limit for our LM CO-undetected grouping is $0.9 \times 10^{10} M_\odot$, which is indeed a lower molecular gas mass than the star forming without CO grouping.

In addition to CO, dust continuum emission has also been used as a proxy for molecular gas mass. S. Alberts et al. (2022) surveyed a cluster population at $z \sim 1.4$ and performed an image stacking analysis on 126 cluster members. The overall dust continuum signal was found to be gas-deficient among galaxies with a positive offset from the SFMS. The two dust continuum stacks, binned into low mass ($\log(M_*/M_\odot) = 10.7 \pm 0.04$) and high-mass ($\log(M_*/M_\odot) = 11.3 \pm 0.05$) groups, have Main Sequence offsets of 0.49 and 0.20 dex, respectively, and have offsets from the field scaling relations of −0.57 and −0.63 dex. This analysis did include cluster members with only photometric redshifts, which could include galaxies that were not a part of a cluster. S. Alberts et al. (2022) comment that including photometric redshift cluster members could dilute their dust continuum signal by including galaxies that were not truly at their photometric redshift. Therefore, the gas-deficient signal could be expected. The stellar masses and SFRs of the $z \sim 1.4$ galaxies are similar to those of our HM-aMS groupings, for which we detect gas masses that are field-like (16 cluster members) and gas-deficient (three cluster members).

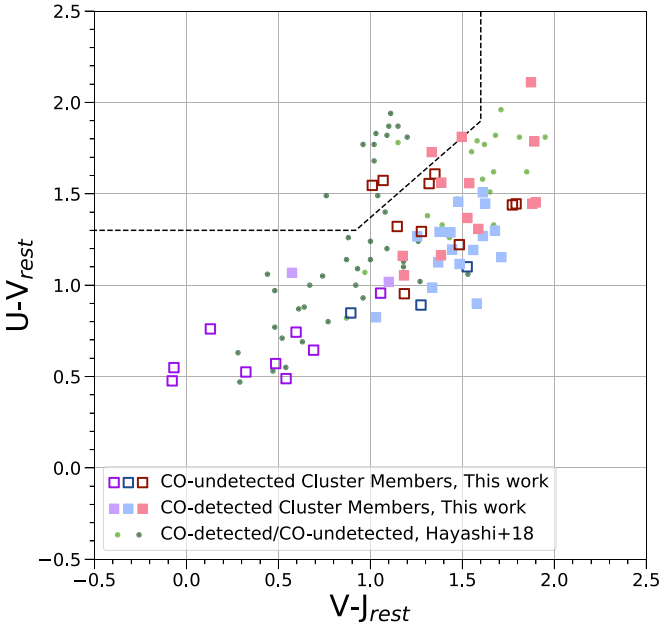

Figure 6. A UVJ diagram of all cluster members. LM galaxies are shown in purple, HM-aMS galaxies in blue, and HM-bMS galaxies in red. Individually CO-undetected and CO-detected galaxies are shown with open and filled points, respectively. Comparable CO-detected and CO-undetected $z = 1.46$ cluster members from M. Hayashi et al. (2018) are shown by the green points and have a mostly similar distribution in UVJ space to the galaxies studied in this work.

Instead of binning by mass, S. K. Betti et al. (2019) group galaxies by their environment, with the highest environmental density classified by >2.6 Mpc^{-2}. All three stacks of dust continuum data are reported as gas-deficient, with the highest density bin having the lowest gas content (−0.42 dex offset in gas fraction from T18), and is consistent with the $z \sim 1.4$ stacks. This bin, despite being considered high density, is ∼6.5× lower density than the spectroscopic detections in the $z = 1.6$ SpARCS clusters. This result and the results from S. Alberts et al. (2022) potentially signify that dust continuum flux consistently underestimates gas mass compared to CO flux. Simulations of high-mass galaxies also suggest that the dust-to-gas ratio becomes highly variable with age as dust is destroyed much faster than molecular gas due to sputtering and other processes (K. E. Whitaker et al. 2021a).

R. Ikeda et al. (2022), in conjunction with M. Hayashi et al. (2018), compared the CO-based and dust continuum-based molecular gas estimates and found statistical agreement for 10 $z = 1.46$ cluster galaxies. However, a robust sample of CO and dust continuum fluxes is needed to establish whether there are systematic corrections needed for the cluster environment when estimating the molecular gas content of galaxies. The work presented in this paper utilizes 21 dust continuum detections that have corresponding CO-fluxes, but we leave the comparison of the molecular gas mass estimates using CO

and dust continuum for a future work (A. Pigarelli et al 2025., in preparation).

6. Conclusion

We present the average molecular gas fractions of cluster galaxies in three $z = 1.6$ galaxy clusters (SpARCS J0224, J0225, and J0330). We employ spectral stacking on nine groupings of 54 cluster members with significant detections in eight of the nine stacks. We also employ a forward modeling analysis to extrapolate the uncertainty of our measured quantities through a molecular gas mass field scaling relation to ascertain whether our measured gas masses are similar to star-forming field galaxies. Our LM and HM-bMS groupings probe a new parameter space of stellar masses and SFRs not covered by other high-redshift spectral stacking and dust continuum stacking studies ($\sim$0.6 dex lower in stellar mass, $\sim$1 dex lower in offset from the SFMS). To date, this is the largest CO study of cluster galaxies below the SFMS at $z > 1$. Our main results are as follows:

1. On average, the ensemble population of CO-detected and CO-undetected cluster galaxies has molecular gas masses consistent with field galaxies within all three of our stellar mass and ΔMS groupings. We see no evidence of significant or systematic molecular gas deficiencies among the ensemble of high-redshift cluster members in contrast to Local Cluster members and stacked high-redshift dust continuum studies. The average gas fraction of galaxies with $\log(M_*/M_\odot) < 10.0$ to be 73% +15/-13%, $\log(M_*) > 10.0$, and $\Delta\text{MS} > -0.3$ dex to be 67% +6/-8%, and $\log(M_*) > 10.0$ and $\Delta\text{MS} < -0.3$ dex to be 34% +9/-7%.
2. We recover a stacked CO(2–1) detection even when breaking down each of our three groupings further into galaxies that are CO-detected and CO-undetected, apart from one LM grouping of CO-undetected galaxies for which we obtain an upper limit. The molecular gas fractions of these groupings range from gas-deficient ($\sim 2\sigma$ below forward-modeled stacks of field galaxies) to gas-rich ($>3\sigma$ above forward-modeled field galaxies), perhaps indicating environmental molecular gas depletion and/or enhanced molecular gas formation. However, this is difficult to disentangle in a population analysis of integrated gas measurements.
3. Specifically, among high-mass galaxies ($\log(M_*) > 10.0$) with $\Delta\text{MS} < -0.3$ dex, we find two stacks with statistically robust differences. There is significant variance from the molecular gas field scaling relation in both the gas-rich and gas-deficient directions for the CO-detected and CO-undetected stacks, respectively. This potentially signifies that environmental processes most strongly affect this population of galaxies.

Many of the SpARCS cluster members also exhibit interesting CO morphologies and kinematics (A. G. Noble et al. 2019; W. J. Cramer et al. 2023); as such, we save further study of this and spatially resolved deviations from scaling relations for future work. In addition, future studies involving the comparison of CO and dust continuum fluxes, as well as the study of the molecular gas content of field galaxies below the SFMS, will further elucidate the effect of environment on molecular gas.

Acknowledgments

This work was supported in part by the NRAO Student Observing Support (SOS) award SOSPADA-024. A.N. additionally acknowledges support from the National Science Foundation through grant AST-2307877, from HST programs GO-16300 and GO-17439, and from the Beus Center for Cosmic Foundations at Arizona State University. Support for program Nos. GO-16300 and GO-17439 were provided by NASA through grants from the Space Telescope Science Institute, which is operated by the Association of Universities for Research in Astronomy, Incorporated, under NASA contract NAS5-26555.

G.W. gratefully acknowledges support from the National Science Foundation through grant AST-2205189. The work of C.C.W. is supported by NOIRLab, which is managed by the Association of Universities for Research in Astronomy (AURA) under a cooperative agreement with the National Science Foundation.

Y.M.B. acknowledges support from UK Research and Innovation through a Future Leaders Fellowship (grant agreement MR/X035166/1).

This paper makes use of the following ALMA data: ADS/JAO.ALMA #2017.1.01228.S, ADS/JAO.ALMA #2018.1.00974.S, ADS/JAO.ALMA #2021.1.01002.S, ADS/JAO.ALMA #2021.1.01257.S. ALMA is a partnership of ESO (representing its member states), NSF (USA) and NINS (Japan), together with NRC (Canada), NSTC and ASIAA (Taiwan), and KASI (Republic of Korea), in cooperation with the Republic of Chile. The Joint ALMA Observatory is operated by ESO, AUI/NRAO, and NAOJ.

ORCID iDs

Alex Pigarelli https://orcid.org/0000-0001-9369-6921
Allison Noble https://orcid.org/0000-0003-1832-4137
Gregory Rudnick https://orcid.org/0000-0001-5851-1856
William Cramer https://orcid.org/0000-0003-0289-2674
Stacey Alberts https://orcid.org/0000-0002-8909-8782
Yannick Bahe https://orcid.org/0000-0002-3196-5126
Patrick S. Kamieneski https://orcid.org/0000-0001-9394-6732
Sebastian Montaño https://orcid.org/0009-0004-0000-9539
Adam Muzzin https://orcid.org/0000-0002-9330-9108
Julie Nantais https://orcid.org/0000-0002-7356-0629
Sarah Saavedra https://orcid.org/0009-0009-9329-1612
Eelco van Kampen https://orcid.org/0000-0002-6327-5154
Tracy Webb https://orcid.org/0000-0002-0104-9653
Christina C. Williams https://orcid.org/0000-0003-2919-7495
Gillian Wilson https://orcid.org/0000-0002-6572-7089
H. K. C. Yee https://orcid.org/0000-0003-4935-2720

References

Alberts, S., Adams, J., Gregg, B., et al. 2022, ApJ, 927, 235
Alberts, S., & Noble, A. 2022, Univ, 8, 554
Aravena, M., Carilli, C. L., Salvato, M., et al. 2012, MNRAS, 426, 258
Betti, S. K., Pope, A., Scoville, N., et al. 2019, ApJ, 874, 53
Bezanson, R., Spilker, J. S., Suess, K. A., et al. 2022, ApJ, 925, 153
Bolatto, A. D., Wolfire, M., & Leroy, A. K. 2013, ARA&A, 51, 207
Boquien, M., Burgarella, D., Roehlly, Y., et al. 2019, A&A, 622, A103
Boselli, A., Fossati, M., & Sun, M. 2022, A&ARv, 30, 3
Brown, T., Wilson, C. D., Zabel, N., et al. 2021, ApJS, 257, 21
Bruzual, G., & Charlot, S. 2003, MNRAS, 344, 1000
Calzetti, D., Armus, L., Bohlin, R. C., et al. 2000, ApJ, 533, 682
Carilli, C. L., & Walter, F. 2013, ARA&A, 51, 105

Castignani, G., Pandey-Pommier, M., Hamer, S. L., et al. 2020, A&A, 640, A65
Chabrier, G. 2003, PASP, 115, 763
Coogan, R. T., Daddi, E., Sargent, M. T., et al. 2018, MNRAS, 479, 703
Cormier, D., Madden, S. C., Lebouteiller, V., et al. 2014, A&A, 564, A121
Cortese, L., Catinella, B., & Smith, R. 2021, PASA, 38, e035
Cowie, L. L., & Songaila, A. 1977, Natur, 266, 501
Cramer, W. J., Kenney, J. D. P., Cortes, J. R., et al. 2020, ApJ, 901, 95
Cramer, W. J., Kenney, J. D. P., Tonnesen, S., et al. 2021, ApJ, 921, 22
Cramer, W. J., Noble, A. G., Massingill, K., et al. 2023, ApJ, 944, 213
Cramer, W. J., Noble, A. G., Rudnick, G., et al. 2024, ApJ, 975, 144
Cybulski, R., Yun, M. S., Erickson, N., et al. 2016, MNRAS, 459, 3287
Daddi, E., Dannerbauer, H., Liu, D., et al. 2015, A&A, 577, A46
Dressler, A. 1980, ApJ, 236, 351
Dressler, A. 1984, ARA&A, 22, 185
Dressler, A., Oemler, A. J., Couch, W. J., et al. 1997, ApJ, 490, 577
Geach, J. E., Smail, I., Coppin, K., et al. 2009, MNRAS, 395, L62
Geach, J. E., Smail, I., Moran, S. M., et al. 2011, ApJL, 730, L19
Genzel, R., Tacconi, L. J., Lutz, D., et al. 2015, ApJ, 800, 20
Gunn, J. E., & Richard, G. J., III 1972, ApJ, 176, 1
Hayashi, M., Tadaki, K.-i., Kodama, T., et al. 2018, ApJ, 856, 118
Hayden, B., Rubin, D., Boone, K., et al. 2021, ApJ, 912, 87
Ikeda, R., Tadaki, K.-i., Iono, D., et al. 2022, ApJ, 933, 11
Jáchym, P., Sun, M., Kenney, J. D. P., et al. 2017, ApJ, 839, 114
Leroy, A. K., Hughes, A., Liu, D., et al. 2021, ApJS, 255, 19
Lewis, I., Balogh, M., De Propris, R., et al. 2002, MNRAS, 334, 673
McMullin, J. P., Waters, B., Schiebel, D., Young, W., & Golap, K. 2007, in ASP Conf. Ser. 376, Astronomical Data Analysis Software and Systems XVI, ed. R. A. Shaw, F. Hill, & D. J. Bell (San Francisco, CA: ASP), 127
Moretti, A., Paladino, R., Poggianti, B. M., et al. 2020a, ApJ, 889, 9
Moretti, A., Paladino, R., Poggianti, B. M., et al. 2020b, ApJL, 897, L30
Moretti, A., Serra, P., Bacchini, C., et al. 2023, ApJ, 955, 153
Muzzin, A., Wilson, G., Demarco, R., et al. 2013, ApJ, 767, 39
Muzzin, A., Wilson, G., Yee, H. K. C., et al. 2009, ApJ, 698, 1934
Nantais, J., Wilson, G., Muzzin, A., et al. 2020, MNRAS, 499, 3061
Nantais, J. B., van der Burg, R. F. J., Lidman, C., et al. 2016, A&A, 592, A161
Noble, A. G., McDonald, M., Muzzin, A., et al. 2017, ApJL, 842, L21
Noble, A. G., Muzzin, A., McDonald, M., et al. 2019, ApJ, 870, 56
Nulsen, P. E. J. 1982, MNRAS, 198, 1007
Oliver, S. J., Bock, J., Altieri, B., et al. 2012, MNRAS, 424, 1614
Peng, Y. J., Lilly, S. J., Kovač, K., et al. 2010, ApJ, 721, 193
Poggianti, B. M., Moretti, A., Gullieuszik, M., et al. 2017, ApJ, 844, 48
Postman, M., & Geller, M. J. 1984, ApJ, 281, 95
Roberts, I. D., & Parker, L. C. 2020, MNRAS, 495, 554
Roberts, I. D., van Weeren, R. J., Timmerman, R., et al. 2022, A&A, 658, A44
Roseboom, I. G., Oliver, S. J., Kunz, M., et al. 2010, MNRAS, 409, 48
Rudnick, G., Hodge, J., Walter, F., et al. 2017, ApJ, 849, 27
Sinigaglia, F., Elson, E., Rodighiero, G., & Vaccari, M. 2022, MNRAS, 514, 4205
Smith, A. J., Wang, L., Oliver, S. J., et al. 2012, MNRAS, 419, 377
Solomon, P. M., & Vanden Bout, P. A. 2005, ARA&A, 43, 677
Speagle, J. S. 2020, MNRAS, 493, 3132
Speagle, J. S., Steinhardt, C. L., Capak, P. L., & Silverman, J. D. 2014, ApJS, 214, 15
Spérone-Longin, D., Jablonka, P., Combes, F., et al. 2021, A&A, 654, A69
Spilker, J., Bezanson, R., Barišić, I., et al. 2018, ApJ, 860, 103
Tacconi, L. J., Genzel, R., Saintonge, A., et al. 2018, ApJ, 853, 179
Vollmer, B., Wong, O. I., Braine, J., Chung, A., & Kenney, J. D. P. 2012, A&A, 543, A33
Wagg, J., Pope, A., Alberts, S., et al. 2012, ApJ, 752, 91
Wang, L., Viero, M., Clarke, C., et al. 2014, MNRAS, 444, 2870
Whitaker, K. E., Narayanan, D., Williams, C. C., et al. 2021a, ApJL, 922, L30
Whitaker, K. E., Williams, C. C., Mowla, L., et al. 2021b, Natur, 597, 485
Williams, C. C., Alberts, S., Spilker, J. S., et al. 2022, ApJ, 929, 35
Williams, C. C., Spilker, J. S., Whitaker, K. E., et al. 2021, ApJ, 908, 54
Wilson, G., Muzzin, A., Yee, H. K. C., et al. 2009, ApJ, 698, 1943
Woodrum, C., Williams, C. C., Rieke, M., et al. 2022, ApJ, 940, 39
Zabel, N., Brown, T., Wilson, C. D., et al. 2022, ApJ, 933, 10
Zabel, N., Davis, T. A., Smith, M. W. L., et al. 2019, MNRAS, 483, 2251